Suspension-Driven gravity surges on horizontal surfaces: Effect of the initial shape

Nadim Zgheib, Thomas Bonometti, Sivaramakrishnan Balachandar

To cite this version:

Nadim Zgheib, Thomas Bonometti, Sivaramakrishnan Balachandar. Suspension-Driven gravity surges on horizontal surfaces: Effect of the initial shape. Computers and Fluids, 2017, 158, pp.84-95. 10.1016/j.compfluid.2017.03.016 . hal-03514461

HAL Id: hal-03514461
https://hal.science/hal-03514461v1

Submitted on 6 Jan 2022

To link to this article : DOI:10.1016/j.compfluid.2017.03.016
URL : https://doi.org/10.1016/j.compfluid.2017.03.016

To cite this version : Zgheib, Nadim and Bonometti, Thomas and Balachandar, Sivaramakrishnan *Suspension-Driven gravity surges on horizontal surfaces: Effect of the initial shape.* (2017) Computers and Fluids, vol. 158. pp. 84-95. ISSN 0045-7930 Item availablity restricted.

Suspension-Driven gravity surges on horizontal surfaces: Effect of the initial shape

N. Zgheib [a,b,*], T. Bonometti [b], S. Balachandar [a]

[a] Department of Mechanical and Aerospace Engineering, University of Florida, Gainesville, FL 32611, USA
[b] Institut de Mécanique des Fluides de Toulouse (IMFT) - Université de Toulouse, CNRS-INPT-UPS, Toulouse, France

Keywords:
Direct numerical simulations
Geophysical flows
Non-canonical
Particle-laden
Deposit

ABSTRACT

We present results from highly resolved direct numerical simulations of canonical (axisymmetric and planar) and non-canonical (rectangular) configurations of horizontal suspension-driven gravity surges. We show that the dynamics along the initial minor and major axis of a rectangular release are roughly similar to that of a planar and axisymmetric current, respectively. However, contrary to expectation, we observe under certain conditions the final extent of the deposit from finite releases to surpass that from an equivalent planar current. This is attributed to a converging flow of the particle-laden mixture toward the initial minor axis, a behaviour that was previously reported for scalar-driven currents on uniform slopes [31]. This flow is observed to be correlated with the travelling of a perturbation wave generated at the extremity of the longest side that reaches the front of the shortest side in a finite time. A semi-empirical explicit expression (based on established relations for planar and axisymmetric currents) is proposed to predict the extent of the deposit in the entire x-y plane. Finally, we observe that for the same initial volume of a suspension-driven gravity surge, a release of larger initial horizontal aspect-ratio is able to retain particles in suspension for longer periods of time.

1. Introduction

Gravity currents are primarily horizontal flows that are driven by a streamwise pressure gradient induced by the difference in density between the current and the ambient. Of particular interest to the present work are sediment-laden or suspension-driven currents where the density difference is due to the suspended sediments. An important feature of suspension-driven currents is their active interaction with the bed. Depending on the intensity and erosive power of the current and on the availability and size of sediments on the bed, a suspension-driven current can be in net-depositional, net-erosive or by-pass mode. In contrast to suspension-driven currents, scalar gravity currents, which are driven by temperature or salinity induced density difference, are conservative since the source of density difference is conserved over time.

Both scalar and suspension-driven currents are actively studied in their canonical geometric configurations of planar and cylindrical releases (see Fig. 1 for schematics of the planar and cylindrical releases). These canonical setups have been extensively researched [14,16,18–22,24,27] resulting in the development of a wide range of simple yet robust models. Indeed, one of the advantages of dealing with a simple geometric configuration is that at times the dimensional space may be reduced to two or even a single dimension making the derivation of elegant theoretical solutions possible. One model that has been particularly popular is the Navier–Stokes-based shallow water equations [12,17,26,28].

Along with the box model [16], the shallow water equations form a powerful tool in the sense that they have the ability to produce simple algebraic scaling relations to predict certain key aspects of gravity currents. For example, the extent of the deposit of a suspension-driven gravity surge initially confined within a circular cylinder may be expressed in terms of the initial parameters: cylinder dimensions, particle settling velocity, and particle volume fraction [4]. A similar relation exists for the extent of the deposit resulting from a planar, lock-release suspension-driven current as well [5,10]. The scaling relations that have proven very useful in the context of planar and cylindrical releases are however not readily extendable to more complex configurations.

A planar or axisymmetric release (see Fig. 1) is defined only by the initial vertical cross-section whose shape is characterized by the height to length (or height to radius) aspect ratio. For non-canonical finite releases, the horizontal cross-section of the release (or the shape of the release) must be additionally defined. In case of a rectangular or elliptic horizontal cross-section, these shapes can be characterized in terms of the initial length to width aspect

---

[*] Corresponding author: Department of Mechanical and Aerospace Engineering, University of Florida, Gainesville, FL 32611, USA.

E-mail address: nzgheib@ufl.edu (N. Zgheib).

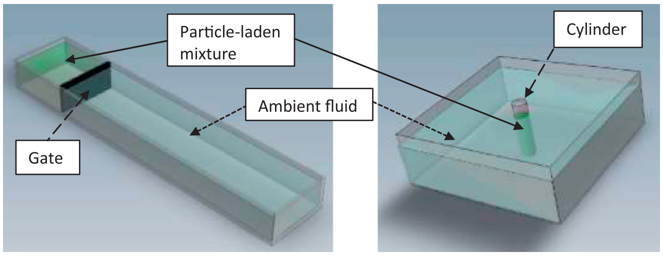

Fig. 1. Schematic of a planar (left) and an axisymmetric (right) configuration. In the planar setup, the particle-laden mixture is initially confined behind a gate whereas in the axisymmetric setup, the mixture is initially confined inside a hollow circular cylinder.

ratio. Zgheib et al. [29] observed that the horizontal cross-sectional shape of the initial release is an important factor which heavily influences the speed and direction of spreading. From both experiments and direct numerical simulations, they observed strong azimuthal dependence along the current-ambient interface in terms of the front velocity. This study was later extended to suspension-driven gravity surges [30] where the extent of the deposit was also observed to be significantly affected by the initial shape. In their study they assessed the importance of bedload transport in correctly predicting the profile of the deposit as well as the short and long term effects of the inherit initial disturbance in laboratory experiments.

The preferential spreading direction of non-planar and non-circular releases of arbitrary horizontal cross-sections depends primarily on the initial shape of the release. However, in the case of gravity surges spreading over an inclined bottom surface [13,25], the preferential spreading direction is dictated by the presence of the slope. There, the spreading of a heavy fluid, initially confined within a slanted circular cylinder, down a uniform slope breaks axisymmetry, and a three-dimensional self-similar shape was seen to evolve. Zgheib et al. [31] observed gravity surges on sloping boundaries to exhibit a converging phase of spreading where the fluid near the head of the current converged toward the symmetry plane. During this phase, the velocity within the head of the current exhibits a strong spanwise component. The relative amplitude of this spanwise component is magnified with steeper slopes, and vanishes, as expected, when the bottom inclination becomes horizontal. These findings on the effects of initial shape and bottom inclination will prove to be important for the present analysis.

Some of the real-world applications of non-canonical suspension-driven gravity currents include dredging, landslides, and building demolitions. In the case of dredging, it is often important to know how the extent of the deposit relates to the conditions at the time of release so that the accurate placement of the dredged material becomes possible. Similarly, in the case of a controlled building demolition, the resulting debris cloud, which constitutes a gravity surge, is inherently related to the geometric properties of the building among other parameters.

The purpose of the present study is to investigate the dynamics of non-canonical suspension-driven gravity surges resulting from rectangular initial releases of various horizontal aspect ratios. The currents to be considered are in the net-depositional regime and therefore after a well-defined period the suspended sediments settle on the bed and the current dies. Based on scaling relations of planar and cylindrical geometries, we propose simple semi-empirical relations which can predict with a reasonable degree of accuracy the shape of the final extent of the deposit for non-canonical releases. We consider large scale simulations of both scalar-driven and suspension-driven gravity surges, whose results are used to test the validity of the semi-empirical relations. In the remainder of the paper, we will use the term scalar-driven to refer to conservative/non-depositional currents (surges with zero settling velocity), the term suspension-driven to refer to non-conservative/depositional currents (surges with non-zero settling velocity), and the term gravity surge to refer to either scalar-driven or suspension-driven currents.

The following sections are organized as follows. In Section 2, we discuss some of the simple relations that have been established for planar and axisymmetric configurations. The mathematical formulation is briefly described in Section 3. In Section 4, we present the main findings of the papers. In Section 5, we propose a semi-empirical expression for predicting the extent of the deposit from rectangular releases. This is followed by an analysis of different scenarios of release depending on the horizontal cross-sectional ratio in Section 6. Finally, conclusions are drawn in Section 7.

2. Theoretical estimates for planar and axisymmetric configurations

The two-layer shallow water model, which is based on the vertically integrated Navier–Stokes equations both in the heavy bottom current and in the ambient, was shown by Bonnecaze et al. [5] to offer a rigorous mathematical approach for the planar suspension-driven gravity surges. Dade and Huppert [11] developed a box model for horizontal suspension-driven currents to obtain simple theoretical estimates of the horizontal extent of the deposit. The characteristic thickness of the deposit and the run-out time were compared against experimental measurements to remarkable success (see also [10]). The run-out time marks the time when the current comes to a full stop as a result of all the particles settling out. Similarly, the run-out distance corresponds to the distance travelled by the current before it comes to a full stop (i.e. the maximum extent of the deposit). Additionally, the characteristic thickness of the deposit refers to the average deposit thickness over the area where the deposit occurs. The key results of the planar box model can be recovered with a scaling argument.

We consider a fixed volume V_0^* of release (per unit width) of particle-laden fluid of initial reduced gravity $g_0'^*$ defined as

$$g_0'^* = g^* \phi_0 \, \frac{\rho_p^* - \rho_a^*}{\rho_a^*}, \tag{1}$$

where ρ_p^* and ρ_a^* denote the particle and ambient fluid densities, respectively, and ϕ_0 is the initial volume fraction of particles in the current. In the above, and for the remainder of the manuscript, the asterisk superscript denotes a dimensional quantity, and zero subscript refers to initial time. For the planar current, the volume of release per unit width of the current can be expressed in terms of the lock height and lock length as $V_0^* = H_0^* \, X_0^*$. We now define the characteristic height of the current to be H^* and the corresponding length of the current to be $X^* = V_0^*/H^*$, which ignores the effects of entrainment or detrainment of ambient fluid or particles into or out of the current. The front velocity of the current scales as $\sqrt{g_0'^* H^*}$ and the characteristic time scale of the collapse is given by the characteristic sedimentation time $T^* = H^*/v_s^*$, where the settling velocity v_s^* is that of a single isolated particle settling in a quiescent ambient fluid. This time roughly corresponds to the time required by a particle to cross a distance equivalent to the initial/characteristic height of the release. We now use the above scaling to properly non-dimensionalize the shallow water concentration equation

$$\frac{\partial \phi}{\partial t^*} + u^* \frac{\partial \phi}{\partial x^*} = -v_s^* \frac{\phi}{h^*}. \tag{2}$$

where u^* is the local horizontal velocity in the current, ϕ is the local volume fraction of particles and h^* is the local height of the current. In particular, we demand the resulting non-dimensional equation to be independent of v_s^*, which yields the condition

$$\frac{v_s^*}{H^*} = \frac{\sqrt{g_0^{'*} H^*}}{X^*}. \tag{3}$$

This is equivalent to assuming that the characteristic time of sedimentation T^* is of the same order of magnitude as the characteristic time of propagation $X^*/\sqrt{g_0^{'*} H^*}$. Substituting for X^* and rearranging we obtain $H^* = (v_s^{*2} V_0^{*2}/g_0^{'*})^{1/5}$ from which we can obtain X^* and T^*. The above scales can be shown to properly non-dimensionalize the shallow water mass and streamwise momentum balances as well. Thus, in the case of a planar current the appropriate scaling of the run-out distance (X_{pd}^*), run-out time (T_{pd}^*), and characteristic deposit height (H_{pd}^*) are

$$X_{pd}^* \sim \left(\frac{g_0^{'*} V_0^{*3}}{v_s^{*2}} \right)^{1/5}, \quad T_{pd}^* \sim \left(\frac{V_0^{*2}}{g_0^{'*} v_s^{*3}} \right)^{1/5}, \quad H_{pd}^* \sim \frac{\phi_0}{\phi_b} \left(\frac{v_s^{*2} V_0^{*2}}{g_0^{'*}} \right)^{1/5}, \tag{4}$$

where ϕ_0 is the initial volumetric particle concentration of the release and ϕ_b is the final volumetric particle concentration within the deposit, which can be taken to be around 0.5 following Dade and Huppert [10]. In the above the subscript "*pd*" stands for planar deposit. Based on comparison against experimental measurements and shallow water solutions, Dade and Huppert [10] recommended the constants of proportionality in the above relations to be 3, 2 and 1/3, respectively.

The scaling analysis for the axisymmetric suspension-driven surge was presented by Bonnecaze et al. [4]. Here the volume of the cylindrical release is given by $V_0^* = \pi R_0^{*2} H_0^*$, where again R_0^* and H_0^* are the initial radius and height of the cylindrical release. In an axisymmetric current the radius of the current, in terms of the characteristic height of the current, goes as $R^* = \sqrt{V_0^*/(\pi H^*)}$. The scaling of the front velocity and time remain the same as in the planar release. We again use the same scales to properly non-dimensionalize the shallow water governing equations, which now yields the condition

$$\frac{v_s^*}{H^*} = \frac{\sqrt{g_0^{'*} H^*}}{R^*}. \tag{5}$$

Substituting for R^* and rearranging we now obtain $H^* = (v_s^{*2} V_0^* / \ (\pi g_0^{'*}))^{1/4}$ from which we can obtain R^* and T^*. The appropriate scaling in the case of a cylindrical deposit of the run-out distance (R_{cd}^*), run-out time (T_{cd}^*), and characteristic deposit height (H_{cd}^*) are

$$R_{cd}^* \sim \left(\frac{g_0^{'*} V_0^{*3}}{v_s^{*2}} \right)^{1/8}, \quad T_{cd}^* \sim \left(\frac{V_0^*}{g_0^{'*} v_s^{*2}} \right)^{1/4}, \quad H_{cd}^* \sim \frac{\phi_0}{\phi_b} \left(\frac{v_s^{*2} V_0^*}{g_0^{'*}} \right)^{1/4}, \tag{6}$$

In the above the subscript "*cd*" stands for cylindrical deposit. Based on comparison against experimental measurements and shallow water solutions, Bonnecaze et al. [4] found the constant of proportionality for the run-out radius to be 1.9. In the case of a full depth release they also observed the above scaling to be valid only when the initial release satisfied the following condition

$$R_0^* \left(\frac{v_s^{*2}}{g_0^{'*} V_0^{*3}} \right)^{1/8} \lesssim 0.1. \tag{7}$$

Instead, if the initial release is in a deep ambient then the right hand side of the above condition changes to 0.3. If the initial release violates condition (7) then the run-out radial distance given in (6) is only an upper bound and an empirical lower bound is defined as [4]

$$R_{cd}^* \simeq 0.92 \left(\frac{g_0^{'*3} V_0^{*7}}{v_s^{*6}} \right)^{1/18}. \tag{8}$$

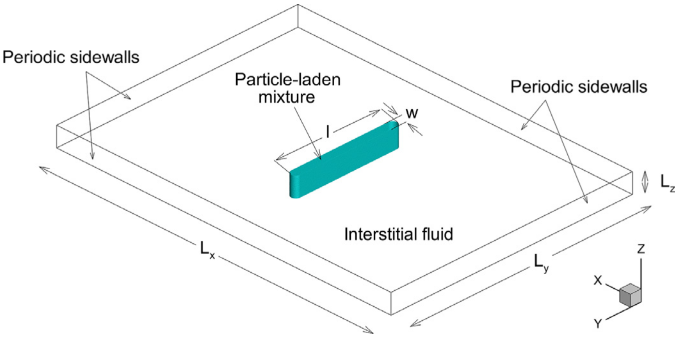

Fig. 2. Computational domain and initial shape of the release (here in the case $\chi_0 = \frac{l}{w} = 12$). We consider a lock-exchange configuration, that is the initial height of the gravity surge H_0^* is equal to that of the ambient fluid L_z^*, i.e. $L_z = 1$.

3. Mathematical formulation

We performed a number of simulations for which a sediment-laden mixture confined within a rounded-rectangular cross-sectional cylinder is released on a horizontal boundary (Fig. 2). The sediment-laden mixture is treated as a continuum and a two-fluid formulation is adopted. We follow Cantero et al. [7] by implementing an Eulerian-Eulerian model of the two-phase flow equations. We solve the conservation of mass and momentum equations for the continuum fluid phase, an algebraic equation for the particle phase momentum, as well as the transport equation for the normalized sediment phase concentration field ρ. The non-dimensional system of equations reads

$$\nabla \cdot \boldsymbol{u} = 0, \tag{9}$$

$$\frac{D\boldsymbol{u}}{Dt} = \rho \boldsymbol{e}^g - \nabla \mathrm{p} + \frac{1}{Re} \nabla^2 \boldsymbol{u}, \tag{10}$$

$$\boldsymbol{u}_p = \boldsymbol{u} + v_s \boldsymbol{e}^g, \tag{11}$$

$$\frac{\partial \rho}{\partial t} + \nabla \cdot (\rho \boldsymbol{u}_p) = \frac{1}{Sc\ Re} \nabla^2 \rho. \tag{12}$$

Here $\boldsymbol{u}_p$ and $\boldsymbol{u}$ are the velocities of the particle and continuum fluid phases, respectively. Implicit in Eq. (11), is the assumption that the time scale of the particles is much smaller than the time flow timescales and thus the particle faithfully follows the local fluid velocity except for the vertical drift due to gravitational settling [1,23]. The settling velocity v_s corresponds to the balance between the Stokes drag force, acting on a single spherical particle assuming a small particle Reynolds number, and the buoyancy force. For the present set of simulations, v_s is an input and its value is prescribed in Table 1. $\boldsymbol{e}^g$ is a unit vector pointing in the direction of gravity, and p represents the total pressure field. The variables Sc and Re are the Schmidt and Reynolds numbers defined as

$$Sc = \frac{\nu^*}{\kappa^*}, Re = \frac{L^* U^*}{\nu^*}, \tag{13}$$

where ν^* represents the kinematic viscosity of the continuous phase and κ^* is the effective mass diffusivity of the particle-laden mixture in the ambient fluid. The particle phase concentration is normalized between 0 and 1 as shown in (14), and the length, velocity, and time scales are defined respectively as

$$\begin{cases} L^* = H_0^*, \ U^* = \sqrt{g^* \phi_0 \dfrac{\rho_p^* - \rho_a^*}{\rho_a^*} L^*}, \ T^* = \dfrac{L^*}{U^*}. \\ \rho = \dfrac{\rho^* - \rho_a^*}{\rho_{m0}^* - \rho_a^*} \end{cases} \tag{14}$$

Table 1
Details of the numerical simulations: The shape variable refers to the horizontal cross-sectional shape of the cylinder, which can be either planar (P), circular (C), or rectangular (R). χ_0 is the initial cross-sectional aspect ratio defined as the ratio of the total length ($\boldsymbol{l}$) to total width ($\boldsymbol{w}$) of the release. $\boldsymbol{L_x} \times \boldsymbol{L_y} \times \boldsymbol{L_z}$ and $\boldsymbol{N_x} \times \boldsymbol{N_y} \times \boldsymbol{N_z}$ refer to the domain size and corresponding grid resolution, respectively. $\boldsymbol{v_s}$, $\boldsymbol{Re}$, and $\boldsymbol{Sc}$ are the non-dimensional settling velocity, Reynolds number and Schmidt number, respectively.

Sim #	Shape	χ_0	l	w	$L_x \times L_y \times L_z$	$N_x \times N_y \times N_z$	v_s	Re	Sc
S1	R	12	5.68	0.47	18 × 13 × 1	960 × 694 × 159	0.02	8430	1
S2	R	8	3.78	0.47	18 × 12 × 1	960 × 640 × 159	0.02	8430	1
S3	R	12	5.68	0.47	20 × 16 × 1	1170 × 936 × 179	0	8950	1
S4	P	∞	∞	0.47	20 × 1.5 × 1	1086 × 82 × 159	0.02	8430	1
S5	C	1	0.47	0.47	7 × 7 × 1	380 × 380 × 159	0.02	8430	1
S6	P	∞	∞	0.47	20 × 1.5 × 1	1228 × 122 × 179	0	8950	1
S7*	R	3.8	1.78	0.47	15 × 10 × 1	800 × 534 × 159	0.02	8430	1

* Details of the simulation previously reported in Zgheib et al. [30]

In the above, ρ^* and ρ^*_{m0} represent the local and initial mixture densities, respectively. Here, we consider the Boussinesq approximation of small density difference between the particle-laden mixture and the ambient fluid in that the concentration only appears in the buoyancy term of the momentum equation (first term on the right hand side of (10)). Eqs. (9)–(12) are solved using a spectral code [8,9] within a rectangular computational domain shown in Fig. 2. Periodic boundary conditions are used for all variables in the streamwise, x, and spanwise, y, directions. At the bottom wall ($z = 0$) no-slip and no-penetration boundary conditions and at the top wall ($z = 1$) free-slip and no-penetration boundary conditions are imposed for the continuous phase velocity. As for the dispersed phase concentration field, Neumann and mixed boundary conditions are enforced at the bottom ($z = 0$) and top ($z = 1$) walls, which translate into zero net particle resuspension flux and zero particle net flux, respectively.

$$\left(\frac{\partial \rho}{\partial z}\right)_{z=0} = 0; \quad \left(\frac{1}{Sc\ Re}\frac{\partial \rho}{\partial z} - v_s \rho\right)_{z=1} = 0. \tag{15}$$

The lengths of the domain in the streamwise and spanwise directions are chosen to ascertain that there is uninterrupted development of the gravity current. Details of the numerical simulations are described in Table 1. It was demonstrated in Zgheib et al. [30] that the propagation of the current is not affected by the lateral boundaries of the computational domain as long as the front of the propagating current is one or more current heights from the boundary. In all the simulation cases considered the horizontal extent of the computational domain was chosen to be large enough to satisfy the above criterion. The grid resolution for suspension-driven and scalar-driven surges is the same as that used in Zgheib et al. [29,30] for rectangular releases, where the adequacy of the grid for converged solution has been established. Also the grid resolution employed is consistent with the requirement that the grid spacing must be of the order of $O(ReSc)^{-1/2}$ [2,15]. We use two values for the Reynolds number $Re = 8430$ and $Re = 8950$ for suspension-driven and scalar-driven gravity surges, respectively. The Schmidt number is set to one for all simulations. This is common practice in these types of flows [23]. Furthermore, Bonometti & Balachandar [6] and Necker et al. [23] demonstrate that the effect of the Schmidt number on the flow in the range of Re numbers considered here is not important as long as it is of order 1. We therefore do not expect our results to be sensitive to the precise value of Schmidt number. These Re and Sc number values were also chosen to allow for a meaningful comparison with previously published results (e.g. [29,30]). The time step is chosen such that the Courant number remains below 0.5. We impose a small random disturbance to the initial concentration field to stimulate a faster transition to turbulence. The amplitude of the disturbance amounts to 5% of the density difference between the sediment-laden mixture and the ambient fluid. The initial interface of the concentration field between the sediment-laden mixture and the ambient fluid is smoothened such that the jump from 0 to 1 occurs over a small distance of 3 grid cells.

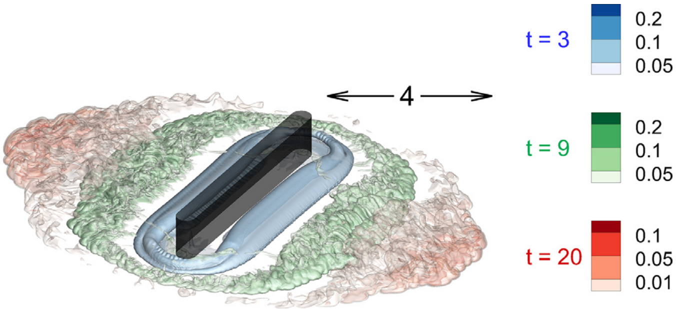

Fig. 3. Flow visualization of S1 using semi-transparent isosurfaces of concentration (ρ) at three time instances, $t = 3$ (blue), 9 (green), and 20 (red). We observe strong azimuthal dependence for which the current is noticeably the weakest along the initial longer axis. A length scale of 4 non-dimensional units is shown above the isosurfaces. (For interpretation of the references to colour in this figure legend, the reader is referred to the web version of this article.)

4. Results

4.1. Rectangular vs planar or axisymmetric suspension-driven gravity surges

In a planar configuration, the gravity surge does not have any mean spanwise motion and is restricted to flow in a single direction along the channel length. Similarly, in an axisymmetric configuration, the flow is radially outward with no mean azimuthal motion. In both cases the final deposit pattern remains statistically planar and axisymmetric, respectively. The three-dimensional spatio-temporal evolution of a current of initial horizontal rectangular shape is presented in Fig. 3. The surge is visualized by multiple semi-transparent isosurfaces of the concentration field ρ at three time instances $t = 3,\ 9$ and 20. The current exhibits strong azimuthal dependence and is the most (resp. least) energetic along the initial shorter (resp. longer) axis. In other words, for rectangular configurations, the initial shape dictates the preferential spreading direction of the current, and as a result the final deposit exhibits azimuthal dependency in both the extent and the areal density. In particular, the current extends the farthest along its initial minor/short axis and propagates the shortest distance along its initial major/long axis.

For a scalar-driven gravity surge, Zgheib et al. [29] observed that at early times a rectangular release advances along its initial minor axis at a speed equivalent to that of an effective planar current if one takes the initial lock length of the latter as half the width of the rectangular release, and the height equal to that of

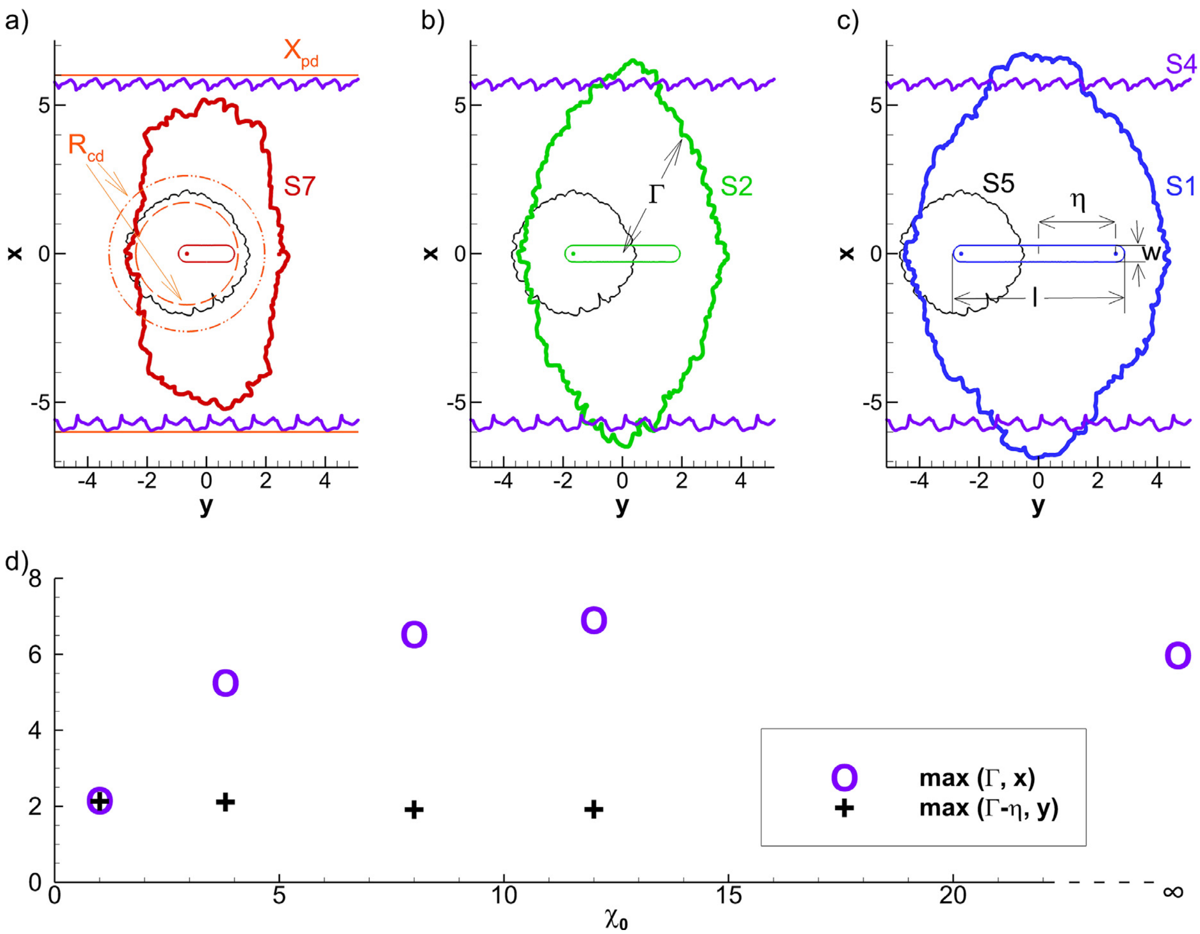

Fig. 4. Final extent of the deposit for the depositional cases in Table 1. For a meaningful comparison with S5, the centre of the cylindrical release was shifted by $-\boldsymbol{\eta}$ units in the $\boldsymbol{y}$-direction to coincide with the geometric centre of the rounded portion of the rectangle (circular dot in frames a, b, and c). The empirical lower bound in (8) for $\boldsymbol{R_{cd}}$ is needed because condition (7) is not met. (d) Maximum extent of the deposit $\boldsymbol{\Gamma}$ (see frame b) along the $\boldsymbol{x}$ and $\boldsymbol{y}$ axes as a function of $\boldsymbol{\chi_0}$. For a meaningful comparison, $\boldsymbol{\Gamma}$ has been shifted by $-\boldsymbol{\eta}$ units along the $\boldsymbol{y}$-axis. For comparison, the maximum extent predicted by (4) for the planar $\chi_0 = \infty$ case is 6.0, while those predicted by (6) and (8) for the axisymmetric $\chi_0 = 1$ case are 2.6 and 1.7, respectively.

the rectangular release. On the other hand, along the initial major axis the current was observed to spread as an effective axisymmetric current of lock radius equal to half the width of the initial rectangular release, and of similar height.

In order to test if the above observations extend to suspension-driven gravity surges, fully resolved direct numerical simulations have been conducted here. These simulations are fully resolved only at the macroscale in the computation of the continuum Eqs. (9)–(12), but they do not resolve the flow at the microscale around individual sediments. When the particle settling velocity is much smaller than the characteristic velocity of the large scale flow, i.e. $v_s^* \ll \sqrt{g_0'^* H_0^*}$, or equivalently $v_s \ll 1$, a suspension-driven gravity surge is likely to behave as a scalar-driven surge to leading order. The simulations consisted of suspension-driven rectangular releases with different initial cross-sectional aspect ratios χ_0, defined as the ratio of the longest to the shortest side, along with simulations in planar and axisymmetric configurations. Some scalar-driven releases were also performed for comparison. It should be noted that the initial cross-sectional shape of the release in the present study is a rectangle in which the short edges have been replaced with semi-circles, thus they are rounded rectangles. The spreading is however nearly identical to a true rectangle with right-angled corners (see Fig. 19 in [29]), and therefore the subsequent discussion is equally applicable to "true" right-angled rectangles.

Fig. 4 shows the extent of the deposit for the suspension driven rectangular surges and how they compare to the planar and axisymmetric configurations. The extent of the deposit in the rectangular release along the initial minor axis (x-axis) can be directly compared with the corresponding deposit for a planar release. For a meaningful comparison along the initial major axis, the centre of the axisymmetric current has been translated to coincide with the centre of the circular portion of the rounded-rectangular configuration. Several observations can be made from Fig. 4: i) the extent of the deposit along the initial major axis agrees reasonably well with that of an axisymmetric release irrespective of the initial horizontal cross-sectional aspect ratio χ_0. ii) The extent of the deposit along the initial minor axis depends on χ_0, and increases as χ_0 is increased. iii) For relatively large values of the cross-sectional aspect ratio ($\chi_0 \gtrsim 8$) the extent of the deposit seems to reach a sort of plateau. iv) The extent of the deposit along the initial minor axis of the rectangular surges of large χ_0, namely $\chi_0 = 8$ and 12, exceeds that of the planar release by about 9 and 13%, respectively. Fig. 4d shows the maximum extent of the deposit along the x and y axes as a function of χ_0 for the depositional cases in Table 1. When the release is axisymmetric ($\chi_0 = 1$), the maximum extent of the deposit is the same along the x and y axes as expected, however as χ_0 increases, the distance travelled by the current along the x-axis appears to increase whereas that along the y-axis seems to remain unchanged. Interestingly, as we approach the planar limit ($\chi_0 \to \infty$), the maximum value of the extent of the deposit is below that

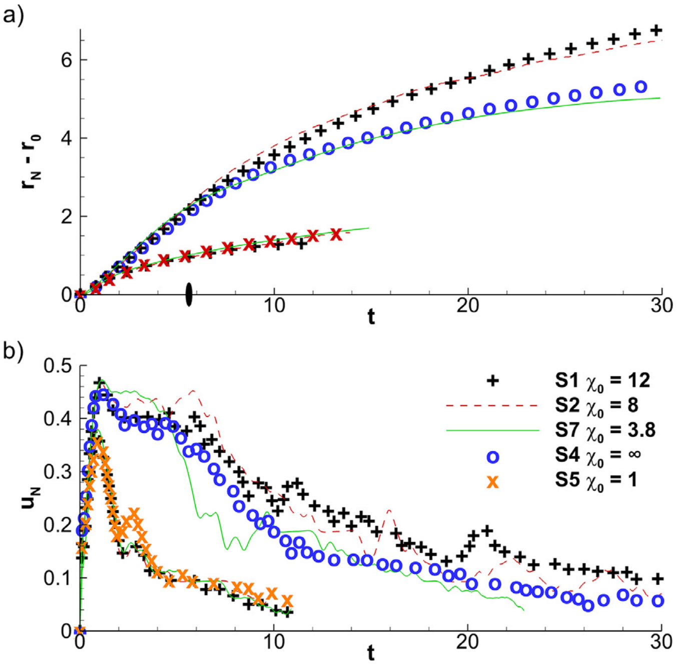

Fig. 5. Temporal evolution of (a) the front position and (b) the front velocity for all suspension-driven gravity surges in Table 1 (the legend in (b) applies to (a)). For rectangular releases, $\boldsymbol{r_N}$ and $\boldsymbol{u_N}$ are shown at both the initial minor ($\boldsymbol{y} = 0$) and major ($\boldsymbol{x} = 0$) axes of the rectangular cross-section. The solid ellipse on the time axis in frame (a) corresponds to the time $\boldsymbol{t} = 6$ where the front evolution of the $\boldsymbol{\chi}_0 = 12$ and $\boldsymbol{\chi}_0 = \infty$ currents begin to diverge from one another.

for $\chi_0 = 8$ and 12 by 9 and 13%, respectively. We will address this somewhat unexpected observation in Section 6.

We may now look at the local dynamics of the front of rectangular surges at some specific locations, namely along the initial minor and major axes. Fig. 5 shows the temporal evolution of the travelled distance along the major and minor axes for some of the simulations shown in Table 1. The dynamics of the front along the initial major axis is observed to be nearly independent of χ_0 and in very good agreement with that of an axisymmetric release both in terms of front position and velocity, as already shown for the final extent of the deposit in Fig. 4. Note that this is in line with the dynamics observed for scalar-driven gravity surges (see e.g. Fig. 14b in [29]).

The dynamics of the front along the initial minor axis is more complicated. Considering the front velocity (Fig. 5b), one can see that the dynamics is similar in the acceleration phase up to time $t = 1$ while in the slumping phase, the mean value of the front velocity u_S and the corresponding duration t_S depend on χ_0. In particular, u_S decreases from 0.45 to 0.40 while t_S increases from 3 to 5, approximately, when χ_0 is increased from 3.8 to 12. Beyond t_S, all the gravity surges experience a deceleration phase of roughly similar trend but for which it is difficult to draw any definite dependency relative to the initial horizontal aspect ratio. Recall that the present front velocity is computed at a specific location of the front contour, and hence the instantaneous variation of the front position, due to the evolution of the lobes and clefts, is likely to introduce some fluctuations in the front velocity, as observed in Fig. 5b. The subtle but noticeable influence of χ_0 observed for the front velocity is also visible in the plots of the time evolution of the front position (Fig. 5a). For instance, the front extent of the $\chi_0 = 3.8$ surge is slightly above the others for times $t \lesssim 6$, then that of the $\chi_0 = 8$ surge is the largest up to $t \lesssim 18$ and finally the $\chi_0 = 12$ surge overcomes the others at later times.

The comparison of front dynamics along the initial minor axis with that of the planar surge is somewhat atypical since the instantaneous front extent of the planar surge is closer to that of the $\chi_0 = 3.8$ surge rather than that of the $\chi_0 = 8$ and $\chi_0 =12$ surges. This is in line with the observation made for the final extent of the deposit in Fig. 4d. Again, this point will be addressed in Section 6.

4.2. *Converging flow in rectangular gravity surges*

As observed in Figs. 4d and 5a, it is somewhat surprising that the finite rectangular releases extend farther or even advance faster than a planar release. Indeed, one may wonder what is the mechanism by which a finite release, whose planform area increases quadratically with size, advances faster or even extends farther than a planar release whose planform increases linearly. A possible explanation can be proposed from the results presented in Fig. 6, where we plot the x and z integrated concentration field, $h_x(y, t)$, defined as

$$h_x(y,t) \;=\int_0^{L_x}\int_0^{L_z}\rho(x,y,z,t)dz\,dx, \tag{16}$$

as a function of y for the suspension-driven (S1 and S4) and scalar-driven (S3 and S6) gravity surges. For the planar release, we further average h_x in the homogeneous y-direction and use it for comparison with the rectangular releases. Because of integration along x and z, the profiles in Fig. 6 are less susceptible to turbulent fluctuations compared to the local concentration field (see Fig. 3). However, in the case of particle-driven surges, as more and more sediments deposit on the bottom wall and exit the computational domain, the mean value of the concentration decreases. Consequently, the fluctuations in the concentration field about the decaying mean concentration value become more pronounced. This could explain the strong symmetry (about $y = 0$) at early times in the profiles of Fig. 6a and the moderate deviation, from symmetry, at later times. On the other hand, because of the conservative nature of the flow for scalar-driven currents, the profiles in frame b remain very symmetric up to the times considered herein.

First, we notice that the mean value of $h_x(y, t)$ decreases over time as a result of sedimentation. It is also clear that the relative amount of dense fluid gradually increases with time at the centre plane ($y = 0$) above that of the corresponding planar release. For instance, the maximum value of h_x is 2%, 11%, and 42% higher than the corresponding average of the planar suspension-driven gravity surge at times $t = 2$, 6 and 10, respectively. This may indicate the presence of a converging flow toward the initial minor axis and supports the observation regarding the faster spreading and longer depositional extent of finite releases (see e.g. Fig. 5). A subtle point that should be stressed is that the converging flow initiates at the two extremities of the rectangle and slowly makes its way toward the initial minor axis ($y = 0$). One may observe that at $t = 2$, $h_x(y, t)$ in the vicinity of the initial minor axis ($|y| < 0.5$) for S1 ($\chi_0 = 12$) is nearly identical to the mean value obtained from the planar case (S4), while $h_x(y, t)$ for $|y| = 1.5$ is noticeably larger than the mean planar value.

The same behaviour is observed for scalar-driven gravity surges (Fig. 6b). A converging flow was also observed in the case of surges spreading on sloping boundaries [31]. In that case, a relatively strong cross-flow velocity component relative to the streamwise velocity component was present and the converging flow was easily identified using a vector plot of the velocity field in the head of the gravity current. This is not the case, however, for rectangular initial releases of suspension-driven gravity surges on horizontal boundaries where the magnitude of the cross-flow velocity component is about an order of magnitude smaller than that of the streamwise component (not shown). Instead, in Fig. 7, we present isocontours of a modified depth-integrated y component of the ve-

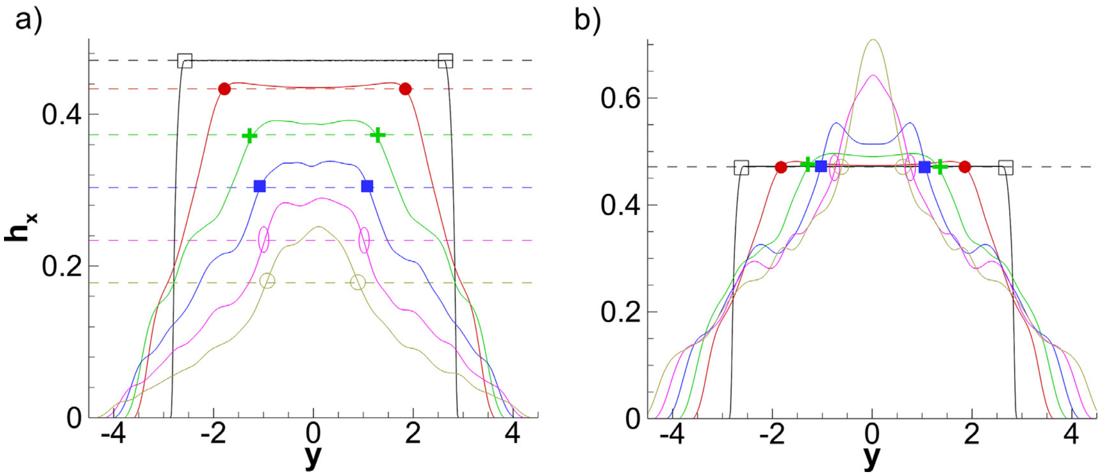

Fig. 6. *x-z* integrated concentration field h_x vs y at $t = 0$ (□), 2(●), 4(+), 6(■), 8(0), and 10(○) for (a) suspension-driven [S1 (solid lines) & S4 (dashed lines)] and (b) scalar-driven [S3 (solid lines) & S6 (dashed lines)] gravity surges. The symbols mark the spanwise locations y where h_x of the $\chi_0 = 12$ current is equal to that of the $\chi_0 = \infty$ planar current.

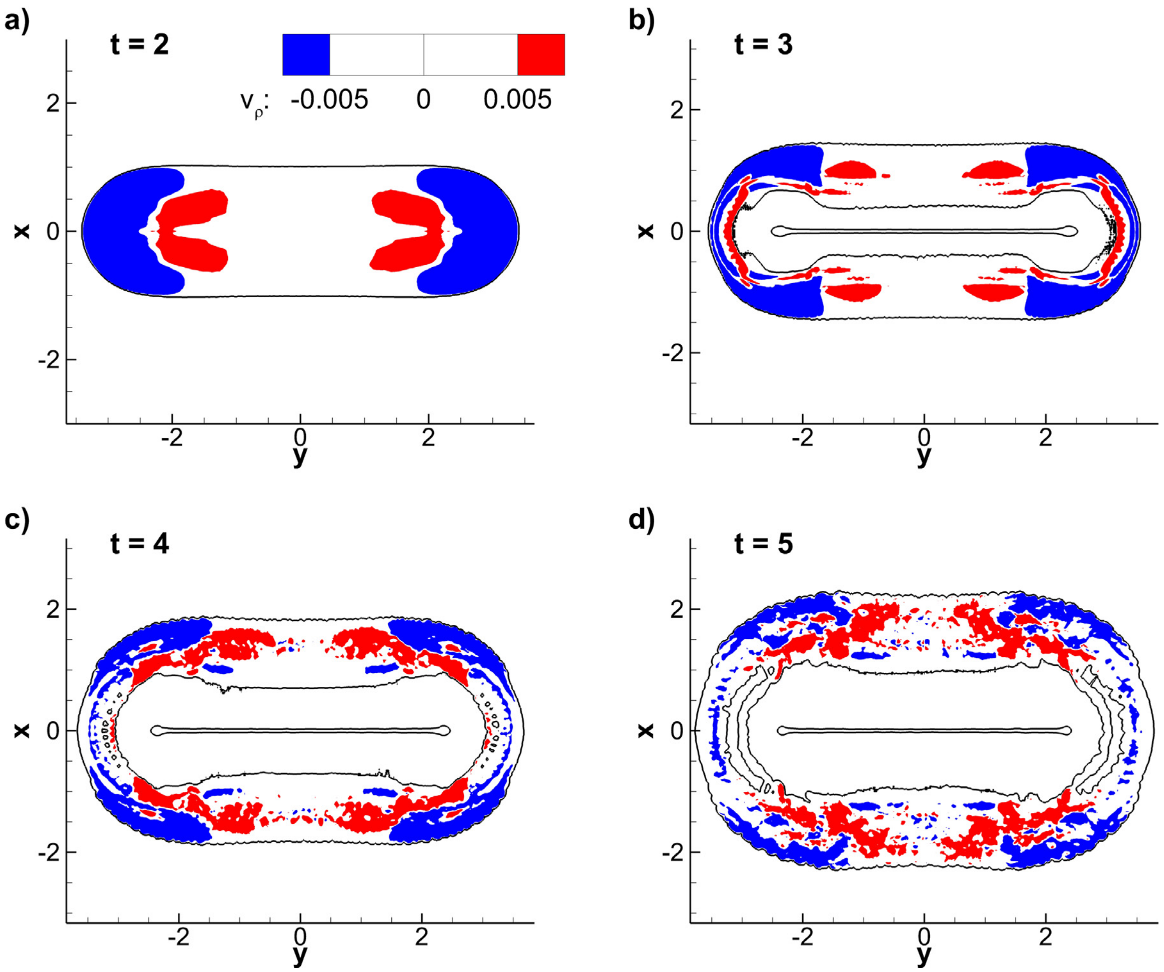

Fig. 7. Contours from S1 in the *x*-*y* plane of the depth-integrated (within the current) y component of the instantaneous velocity field v_ρ (see text for definition). Regions in red corresponds to $v_\rho \geq 5 \times 10^{-3}$ and indicate a converging flow toward the $y = 0$-plane whereas regions in blue corresponds to $v_\rho \leq -5 \times 10^{-3}$ and indicate a diverging flow away from the $y = 0$ plane. The outer black solid line in each frame corresponds to the location of the front and represents the isocontour $h = 5 \times 10^{-2}$ where h is the vertically integrated density field defined as $h = \int_0^{L_z} \rho dz$. (For interpretation of the references to colour in this figure legend, the reader is referred to the web version of this article.)

locity field v_ρ in the x-y plane. In each of the 4 frames in Fig. 7, the isocontours of v_ρ are bounded by an outer solid black line, which corresponds to the location of the front. Here, v_ρ is defined as

$$v_\rho(x, y, t) \; = \frac{-y}{|y|}\int_0^{L_z} \rho v \, dz, \tag{17}$$

where v represents the y component of the three-dimensional velocity field $\boldsymbol{u}$. Therefore, in regions where $v_\rho > 0$, the flow converges toward the symmetry plane $y = 0$ and vice versa. At early times $t = 2$, we can see the presence of two zones of converging flow in the region $1 \leq |y| \leq 2$ within the suspension-driven gravity surge. As time evolves, these regions spread and tend to approach the symmetry plane, such that at time $t = 5$, the flow inside the current located in the region close to the initial minor axis, i.e. $|y| \leq 2$ is mostly oriented toward the symmetry plane $y = 0$. This observation confirms the presence of a converging flow toward the initial minor axis which may be responsible for the mass buildup observed in Fig. 6 initiating at the extremities and propagating toward the plane $y = 0$. Consequently, such a mass buildup may modify the local front velocity since the latter scales as the square-root of the front height [3].

4.3. Travelling informational perturbation along the front contour

One way to track how information travels along the front is to see how certain parameters that are otherwise uniform in space (along the y-axis) for a planar release spatially evolve when the release is of finite size. The normal-to-the-front angle (ϑ) and the normal-to-the-front velocity (u_N) are two such parameters. We choose ϑ as one of the two parameters because it provides information on the instantaneous local spatial and temporal evolution of the front. Another parameter analogous to ϑ that could potentially provide equivalent information is the local curvature of the front. However, to evaluate ϑ only first order derivatives are required, unlike evaluation of the local curvature. Here, $\vartheta(y, t)$ is computed as

$$\vartheta(y, t) \; = \arctan(\partial x_N / \partial y), \tag{18}$$

where, x_N corresponds to the front position in the upper symmetry plane ($x \geq 0$). At the time of release $t = 0, \vartheta(y, 0)$ is such that

$$\begin{aligned} |\vartheta(y, 0)| &= 0 \quad \text{for} \quad |y| < \eta, \\ |\vartheta(y, 0)| &> 0 \quad \text{for} \quad |y| > \eta. \end{aligned} \tag{19}$$

where η is the distance from the geometric centre of the rectangular cross-section to the local centre of the rounded portion of the rectangle (see Fig. 4). To monitor when the flat portion of the front ceases to remain flat, we need to see when $|\vartheta| > \epsilon$, where ϵ is a small number. We therefore need a suitable value of ϵ that is small, to accurately detect the change in the direction of the front as early as possible. However, ϵ must be large enough to obtain a clear signal-to-noise ratio. We find for the present problem, the isovalue $\vartheta = 0.1$ to be a reasonable choice. As for the normal-to-the-front velocity u_N the value $u_N = 0.39$ is chosen as a reference since it is close to the value of the mean slumping velocity of the planar current (see Fig. 5b, S4). This is likely to be the slumping velocity that the flat portion of the rectangular release experiences before the information on the “finiteness” of the release reaches it.

Fig. 8a and b show contours of $|\vartheta|$ and u_N, respectively, in the y-t plane for early times $t \leq 4$, whereas Fig. 8c overlays the isocontours of $\vartheta = 0.1$ and $u_N = 0.39$ on top of the front position in the upper symmetry plane ($x \geq 0$). As time evolves, the region along which the front remains flat ($|\vartheta| \leq 0.1$) and advances at a speed close to that of the planar release ($u_N \geq 0.39$) decreases. The rate at which the flat portion of the release decreases is roughly constant at early times ($t \leq 4$). From Fig. 8a, we can estimate the slope dy/dt of the $|\vartheta| = 0.1$ isocontour to be $dy/dt \approx 0.23$. On the other hand, the slope dy/dt of the $u_N = 0.39$ isocontour is estimated from Fig. 8b to be $dy/dt \approx 0.32$.

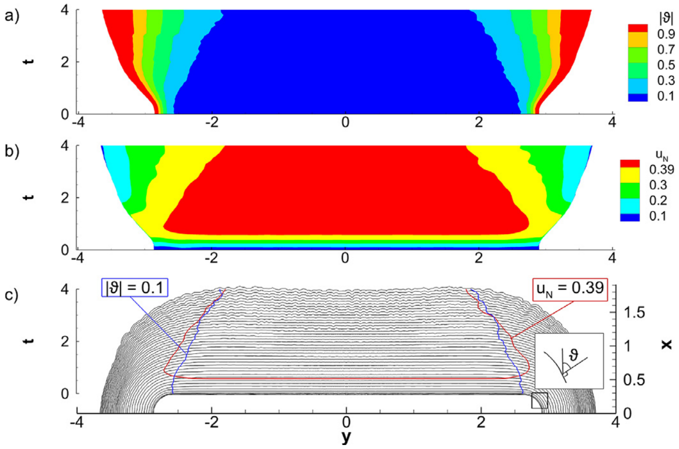

Fig. 8. Contours in the $\boldsymbol{y}$-$\boldsymbol{t}$ plane from S1 of (a) the absolute value of the normal-to-the-front angle $\vartheta = \tan^{-1}(\partial \boldsymbol{x_N}/\partial \boldsymbol{y})$ and (b) the normal-to-the- front velocity $\boldsymbol{u_N}(\boldsymbol{y}, \boldsymbol{t})$. (c) Temporal evolution of the front in the upper symmetry plane ($\boldsymbol{x} \geq 0$) at equal increments in time of ($\boldsymbol{\Delta t} = 0.1$). The thick blue and red lines correspond to the isocontours of $|\vartheta| = 0.1$ and $\boldsymbol{u_N} = 0.39$, respectively. Inset shows schematic of ϑ on the curved portion of the front. (For interpretation of the references to colour in this figure legend, the reader is referred to the web version of this article.)

The isocontours of $\vartheta = 0.1$ and $u_N = 0.39$ are easily extracted at early times ($t \leq 4$) when the front is still relatively smooth. At later times, the front becomes more complex and highly three-dimensional due to the lobe and cleft instability, which makes it more difficult to precisely extract the above isocontours. However, we can obtain a time estimate ($t_{p,\, dy/dt}$) of when the perturbation reaches the symmetry plane ($y = 0$), by assuming that the slope dy/dt remains constant as the perturbation advances inward. We should note nonetheless that this assumption may not necessarily be true, as the perturbation speed may change as it advances. A better estimate may be obtained by marking the time (t_{p,r_N}) when the front position $r_N(t)$ along the x-axis from S1, S2, and S7 exceeds that from S4. From Fig. 5a, we find $t_{p,r_N} \approx 2$, 3, and 6 for S1, S2, and S7, respectively. A comparison of the characteristic perturbation times as well as the characteristic sedimentation and propagation times are shown in Table 2. The observed perturbation time t_{p,r_N} is smaller than the estimated time $t_{p,\, dy/dt}$, which suggests that the perturbation speed does not remain constant, but rather increases at later times ($t > 4$) as it advances inward.

In all the simulations considered herein, the perturbation reaches the symmetry plane ($y = 0$) before the current stops. Indeed, as the perturbation and propagation characteristic times are of the same order, we should expect the converging flow to reach the symmetry plane before the current arrives at a standstill. On the other hand, if the horizontal aspect ratio of the release is very large, i.e. $\chi_0 \gg 1$, the characteristic perturbation time will be correspondingly very large as well, whereas the characteristic propagation time will approach that of the planar release (S4). For such a case, the converging flow will have no effect on the dynamics of the current along the symmetry plane ($y = 0$). As for the characteristic sedimentation time, we observe T_s to be about an order of magnitude larger than the perturbation times $t_{p,\, dy/dt}$ and t_{p,r_N}. This implies that the effect of sedimentation is not likely to be an important factor in the dynamics of the converging flow before it reaches the symmetry plane.

Overall, Fig. 8 clearly shows that the information of the finite size of the release along the y-direction propagates from the corners to the centreline ($y = 0$) along the front. The precise value of the velocity at which this information propagates, however, and

Table 2
Characteristic perturbation, sedimentation, and propagation times from S1, S2, S4, and S7.

Sim #	χ_0	Characteristic perturbation time[#] $t_{p,dy/dt} = [l^*/(dy^*/dt^*)]/T^*$	Characteristic perturbation time[£] t_{p,r_N}	Characteristic sedimentation time $T_s = (H_0^*/v_s^*)/T^*$	Characteristic propagation time $T_p = [\max(\Gamma^*, x)/\sqrt{g_0^{\prime *} H_0^*}]/T^*$
S7	3.8	[2.8 – 3.9]	2	50	5.2
S2	8	[5.9 – 8.2]	3	50	6.5
S1	12	[8.9 – 12.3]	6	50	6.9
S4	∞	∞	–	50	6.0

[#] Both values of dy/dt are considered: $dy/dt|_{\vartheta=0.1}$ and $dy/dt|_{u_N=0.39}$

[£] t_{p,r_N} is the time when the front position along the x-axis from S1, S2, and S7 exceeds that from S4

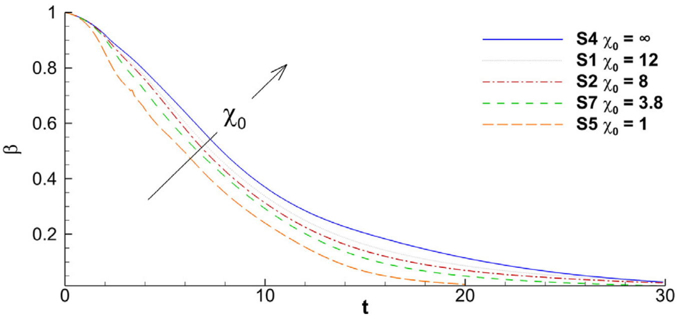

Fig. 9. Retention rate of particles in suspension as a function of time. For the same initial volume of a suspension-driven gravity surge, larger cross-sectional aspect ratio releases are able to retain particles in suspension for longer periods of time.

its dependence on other parameters remain unclear. It should be noted that the slope dy/dt of the $u_N = 0.39$ isocontour also provides some measure for how information travels within the current. The front velocity u_N is related to the current's thickness or height, h_N, by the Froude condition

$$u_N \sim \sqrt{h_N}, \tag{20}$$

and therefore as u_N varies spatially, so must h_N. However, u_N is a much easier quantity to evaluate than h_N, because unlike u_N, there is no clear definition for the front height.

4.4. *Particle rate of retention as a function of χ_0*

One aspect that is of great interest in the study of suspension-driven gravity surges is the depositional rate. It is often very useful to know how long a suspension-driven current can maintain its particles in suspension before coming to a full stop. In Fig. 9, we plot the normalized amount of particles remaining in suspension over time, β, for all suspension-driven simulations in Table 1. β is defined as

$$\beta(t) = \frac{\int_0^{L_x}\int_0^{L_y}\int_0^{L_z} \rho(x,y,z,t)\,dz\,dy\,dx}{\int_0^{L_x}\int_0^{L_y}\int_0^{L_z} \rho(x,y,z,0)\,dz\,dy\,dx}. \tag{21}$$

As expected, circular releases have the lowest retention rate of particles, whereas planar releases have the largest. This is a direct result of the ever diverging spreading nature of axisymmetric releases as compared to the unidirectional spreading of planar currents. In addition, for the same initial volume of a particle-laden mixture, releases with large cross-sectional aspect ratios, χ_0, retain their particles in suspension for longer times. For instance, the value $\beta = 0.15$, which corresponds to the fact that 15% of the particles remain in suspension in the gravity surge, is reached at time $t = 12.1$ and 15.6 for $\chi_0 = 1$ and 12, respectively. Similarly, at time $t = 10$, approximately 24% (resp. 34%) of the particles remain suspended in the gravity surge of horizontal aspect ratio $\chi_0 = 1$ (resp. 12).

5. Predictive models for rectangular suspension-driven gravity surges

5.1. *Final extent of the deposit*

As shown in Fig. 4a, the shallow water theoretical expressions (4)–(6) and the empirical relation (8) predicting the final extent of the deposit for the planar and axisymmetric releases, agree well with the present planar and axisymmetric simulations. For instance, in the planar case, the extent of the deposit from (4) and from the spanwise average of S4 are 5.7 and 6.0, respectively. Similarly, for the axisymmetric release, the azimuthal average of the extent of the deposit S5 is 2.0, which lies between the lower and upper bounds of 1.7 and 2.6 from expressions (8) and (6), respectively. Here, the empirical lower bound is used because the condition in (7) is not met. In addition, these expressions provide a reasonably good estimate for the extent of the deposit along the initial minor and major axes of the rectangular release.

Here we propose an estimate of the extent of the deposit in the entire x-y plane. Zgheib et al. [29] showed that scalar-driven rectangular releases reach a self-similar spreading phase in which the azimuthal variation of the front position may be described by a sinusoidal function of the local angle θ in the polar coordinate system, whose origin coincides with the geometrical centre of the release, θ being measured anticlockwise from the x-axis. We therefore suggest a similar sinusoidal function to describe the extent of the deposit with the help of (4), (6) and (8). The empirical expression describing the extent of the final deposit Γ which is the radial distance between the local front and the geometrical centre reads

$$\Gamma(\theta) = A\sin^n(\theta) + B, \tag{22}$$

with

$$A = \frac{\left|X_{pd}^* - \left(R_{cd}^* + \eta^*\right)\right|}{H_0^*} \quad \text{and} \quad B = \frac{\left(R_{cd}^* + \eta^*\right)}{H_0^*}. \tag{23}$$

where η^* is the distance from the geometric centre of the rectangular cross-section to the local centre of the rounded portion of the rectangle (see Fig. 4), X_{pd}^* is given by (4), and since the condition in (7) is not met, the upper and lower bounds of R_{cd}^* are given by (6) and (8), respectively. Here again, the asterisk superscript denotes a dimensional variable, all other variables are to be understood as non-dimensional. We use the scaling given in (14) to non-dimensionalize (22). The exponent n in (22) is the only fitting parameter of the function.

Fig. 10a shows the extent of the final deposit Γ as a function of θ for S2 along with the theoretical and semi-empirical predictions of R_{cd}^* and X_{cd}^*. The value $n = 6$ was observed to provide the best agreement. Other values of n in the range [4, 8] gave roughly similar results. Similarly, Fig. 10c and d show the extent of the deposit in the x-y plane for S1, S2 and S7 as well as Γ as obtained from (22). It should be noted that for the cases considered in Fig. 10, the condition in (7) does not hold, and R_{cd}^* is bounded by the condi-

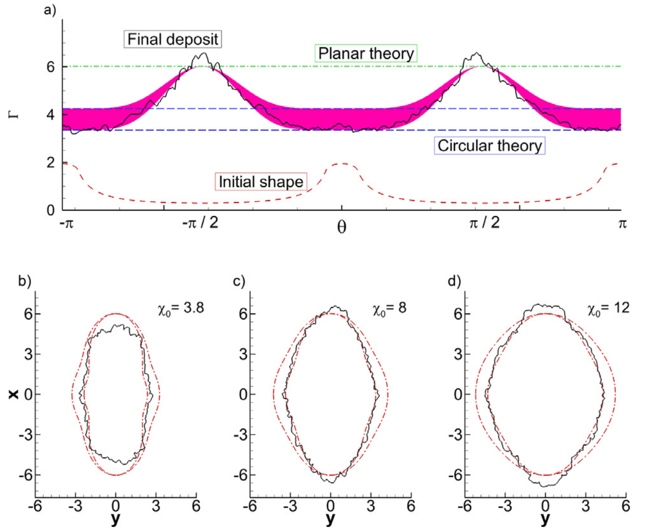

Fig. 10. a) Extent of the final deposit vs the polar coordinate $\boldsymbol{\theta}$ from S2 (thick black line). The pink shaded region is the prediction from (22) using both bounds of the axisymmetric release from (6) and (8). For comparison, the prediction from (4) of the final extent for a planar gravity surge (green horizontal dash-dot line) and those from (6) and (8) for an axisymmetric gravity surge (blue horizontal long dashed lines) are also plotted. (b)-(d): Extent of the final deposit in the $\boldsymbol{x}$-$\boldsymbol{y}$ plane from S7 ($\chi_0 = 3.8$), S2 ($\chi_0 = 8$), and S1 ($\chi_0 = 12$) respectively. The dashed red lines correspond to the prediction from (22) using the upper and lower bounds from (6) and (8). (For interpretation of the references to colour in this figure legend, the reader is referred to the web version of this article.)

tions in (6) and (8) [4]. Good agreement is observed in all 3 cases, the relative discrepancy between the simulated and predicted extents of the deposit along the x axis being approximately -17, 9, and 13%, for $\chi_0 = 3.8$, 8 and 12, respectively. Along the y axis, the extent of the deposit from the simulations lie within the predicted bounds and are closer to the empirical lower bound given in (8).

5.2. *Horizontal aspect ratio of the deposit*

Using (22), one may also predict the final aspect ratio of the deposit χ_∞. Noting that with the present coordinate system the minimum and maximum extent of the deposit correspond to $\theta = 0$ and $\theta = \pi/2$, respectively, we have $\chi_\infty = (A+B)/A = X^*_{pd}/(R^*_{cd} + \eta^*)$. Using the fact that $\chi_0 = (R^*_0 + \eta^*)/R^*_0$, we can eliminate η^* in the expression for χ_∞ and obtain a prediction of the final horizontal aspect ratio of the deposit as a function of the initial geometric parameters, *viz*

$$\chi_\infty = \frac{X^*_{pd}}{R^*_{cd} + R^*_0(\chi_0 - 1)}. \tag{24}$$

A plot of χ_∞ vs χ_0 for the present set of parameters is shown in Fig. 11. For small values of χ_0, (24) performs poorly as expected. Indeed, as the initial cross-sectional aspect ratio tends to unity, one would expect both the “minor” and “major” axis of the release to behave identically as an axisymmetric current and hence $\chi_\infty \approx 1$. In contrast, (24) gives $\chi_\infty \approx X^*_{pd}/R^*_{cd}$ which is larger than unity since with the present model, the initial minor axis of the rectangular release can only exhibit a planar-like type of spreading. On the other hand, for the present set of parameters, as χ_0 is increased, (24) agrees very well with experimental and numerical data. Let us recall that (24) is applicable whenever (4), (6) and (8) are valid, i.e. to a much wider set of parameters than in the present case.

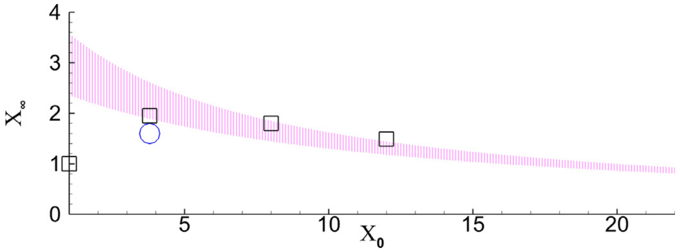

Fig. 11. Final deposit aspect ratio $\boldsymbol{\chi_\infty}$ vs $\boldsymbol{\chi_0}$ for all the suspension-driven simulations (black square symbols) in Table 1. The blue circle corresponds to experiment 1 in Zgheib et al. [30]. The experiment is equivalent to S7 in Table 1. The shaded region corresponds to (24) using the upper and lower bounds in (6) and (8). (For interpretation of the references to colour in this figure legend, the reader is referred to the web version of this article.)

6. Scenarios of dynamics and deposition of a suspension-driven gravity surge

Here, we propose a scenario for the dynamics of a suspension-driven gravity surge of initial arbitrary shape depending on the competition between the characteristic times of sedimentation, propagation, and reflection of the perturbation.

We may now consider the planar and axisymmetric configurations as limiting cases for rectangular cross-sectional releases. When the initial cross-sectional aspect ratio $\chi_0 = 1$, the rectangular release reduces to an approximate axisymmetric circular release. On the other hand, as $\chi_0 \to \infty$, we retrieve the planar release. All other rectangular releases with finite values of χ_0 exhibit a behaviour that is a combination of both canonical releases. That is the broad edge of the rectangular cross-section behaves, at least for some finite initial time, as a planar current, whereas the short edge acts as a diverging axisymmetric release until the current comes to a full stop.

The front along the initial minor axis advances as a planar front until the information of the “finiteness” of the release is received. This can be seen in Fig. 5a as to when the front locations for $\chi_0 = 8$ and 12 separate from that of a planar current. This statement implies that there is an information wave that travels along the front of the current and carries with it the information that the release is of finite length in the y-direction and does not extend indefinitely along the initial major axis.

The reason the final extent of the deposit along the minor and major axes of the rectangular release conforms well to planar and axisymmetric releases is in fact due to the fronts along those specific directions behaving in a similar fashion to their respective canonical currents from the time of the release onward. Fig. 5 shows the temporal evolution of the travelled distance along the major and minor axes for some of the simulations shown in Table 1. The following observations can be made.

i) It confirms that the temporal evolution along the initial major axis is equivalent to that from an axisymmetric release and is nearly independent of χ_0. The same behaviour was observed for scalar-driven currents (Figure 14b in [29]).

ii) There appears to be some critical initial cross-sectional aspect ratio χ_{0cr1} above which the extent of the deposit exceeds that from an equivalent planar current. For the present set of parameters, we observe a value of $\chi_{0cr1} \approx 5$.

iii) There exists another higher initial critical aspect ratio χ_{0cr2}, above which the extent of the deposit along the initial minor axis becomes completely independent of χ_0 and matches exactly the extent from an equivalent planar release. χ_{0cr2} corresponds to an initial release for which the converging flow never reaches the symmetry plane ($y = 0$).

iv) There exists an initial aspect ratio χ_{0max} such that $\chi_{0cr1} < \chi_{0max} < \chi_{0cr2}$ for which the deposit attains its largest possible extent along the initial minor axis.
v) For values of χ_0 below χ_{0max}, the current (along the initial minor axis) experiences a larger slumping (nearly constant) velocity for smaller values of χ_0, but the duration of this nearly constant velocity phase increases as χ_0 increases (see Fig. 5b). The same behaviour was also observed for scalar-driven gravity surges (Figure 14b in [29]).
vi) For values of χ_0 such that $\chi_{0cr1} < \chi_0 < \chi_{0cr2}$, the planar front velocity provides a lower limit to the front velocity along the initial minor axis for the entire duration of the flow. Indeed as seen from Fig. 5b, the front velocity along the initial minor axis from S1 and S2 is always larger than or equal to the corresponding planar release of S4.

Indeed, as χ_0 attains larger and larger values, there comes a point for which the current comes to a full stop before the converging flow ever reaches the symmetry plane ($y = 0$). In that case, the front along the initial minor axis advances as a planar current. Furthermore, as discussed in point (v), rectangular releases with values of χ_0 such that $1 < \chi_0 < \chi_{0max}$, experience a larger slumping (nearly constant) velocity for smaller values of χ_0. This may be due to the fact that for small values of χ_0, the converging flow reaches the initial minor axis earlier when the current is already relatively more energetic than at later times. The converging flow would further increase the thickness of the current and therefore raise the slumping velocity along the initial minor axis (recall that $u_N \sim h_N^{1/2}$).

7. Conclusions

We presented results from highly resolved direct numerical simulations of finite release horizontal gravity surges, both suspension-driven and scalar-driven. Canonical (axisymmetric and planar) and non-canonical (rectangular) configurations were studied, which allowed us to vary the initial horizontal cross-sectional aspect ratio χ_0 over a wide range. The purpose of the study was to build on the knowledge regarding axisymmetric and planar releases and use it to propose simple relations for certain key parameters of rectangular configurations.

We showed that the final extent of the deposit along the initial minor (resp. major) axis of an initially rectangular suspension-driven gravity surge resembles that of a planar (resp. axisymmetric) release with the same initial height and half the width of the rectangular release. In addition, rectangular gravity surges with the same initial volume but with larger χ_0, retain their particles in suspension for longer times compared to surges of smaller χ_0.

A prediction for the final extent of the deposit in the entire x-y plane (and not just along the major and minor axes) was proposed using available theoretical and empirical models for canonical suspension-driven gravity surges. Following Zgheib et al. [29], we proposed a sinusoidal empirical relation (22), for the final extent of the deposit as a function of azimuthal orientation whose amplitude is obtained from previously established relations on axisymmetric and planar currents. Additionally, a simple explicit expression (24), relating the final aspect ratio of the deposit, χ_∞ to the initial cross-sectional aspect ratio of the release, χ_0 was proposed. While the present simulations are based on specific values for the settling velocity as well as the Reynolds and Schmidt numbers, the proposed semi-empirical expressions (22) and (24), because of their inherent coupling with Eqs. (4), (6), and (8), are applicable to a wide range of parameters including the Reynolds and Schmidt numbers, the height and cross-sectional aspect ratio of the release, the particle settling velocity, the particle volume fraction, as well as the initial reduced gravity. Therefore, the expected effects of changing these parameters may be directly inferred from the canonical, semi empirical expressions of (4), (6), and (8). Therefore, with the knowledge of the initial conditions of the release, it is possible to predict the extent of the final deposit of a rectangular release. Conversely, using (22) and (24), one can choose the initial parameters of the release to control the final extent of the deposit.

One of the most counterintuitive outcomes is that contrary to expectation, some suspension-driven gravity surges may advance slightly but noticeably faster and extend farther than equivalent planar surges that exclusively undergo unidirectional spreading (up to 13% of the extent for the present range of parameters). Intuitively, one would expect the final extent of the deposit from planar gravity surges to act as an asymptotic limit to the extent of the deposit along the initial minor axis of rectangular gravity surges. This is shown not to be the case. This unexpected outcome is attributed to a converging flow inside the surge toward the initial minor axis of the rectangular cross-section. A converging flow behaviour was also observed for finite release scalar-driven gravity surges on uniform slopes [31], the intensity of which increases sharply for steeper slopes. This leads us to conjecture that for suspension-driven gravity surges released on a uniform slope, the extent of the deposit along the initial minor axis of a rectangular release might significantly exceed that of a planar release. The discrepancy is expected to be further highlighted as the slopes become steeper.

This converging flow is brought upon by a non-uniform spatial distribution due to the finite nature of the release as opposed to planar releases that extend indefinitely along the y-axis. By tracking the spatiotemporal evolution of otherwise spatially uniform variables for planar releases, we provided some estimate for the speed of propagation of the informational wave and the characteristic time of reflection at the symmetry plane. We do not currently know what parameters control or affect the speed of the perturbation wave. This is an interesting subject that requires further investigation.

Acknowledgements

This research was partly funded by the ExxonMobil Upstream Research grant (EM 09296). We wish to thank the French Embassy in the USA for the Chateaubriand Fellowship as well as the National Science Foundation Partnership for International Research and Education (PIRE) grant (NSF OISE-0968313) for partial support. Some of the computational time was provided by the Scientific Groupment CALMIP (project P1525), the contributions of which is greatly appreciated.

References

[1] Balachandar S, Eaton JK. Turbulent dispersed multiphase flow. Ann Rev Fluid Mech 2010;42:111–33.
[2] Birman V, Martin JE, Meiburg E. The non-Boussinesq lock-exchange problem. Part 2. High-resolution simulations. J Fluid Mech 2005;537:125–44.
[3] Benjamin TB. Gravity currents and related phenomena. J Fluid Mech 1968;31(02):209–48.
[4] Bonnecaze RT, Hallworth MA, Huppert HE, Lister JR. Axisymmetric particle–driven gravity currents. J Fluid Mech 1995;294:93–121.
[5] Bonnecaze RT, Huppert HE, Lister JR. Particle-driven gravity currents. J Fluid Mech 1993;250:339–69.
[6] Bonometti T, Balachandar S. Effect of Schmidt number on the structure and propagation of density currents. Theor Comp Fluid Dyn 2008;22(5):341–61.
[7] Cantero MI, García MH, Balachandar S. Effect of particle inertia on the dynamics of depositional particulate density currents. Comput Geosci 2008;34(10):1307–18.
[8] Cantero M, Lee JR, Balachandar S, Garcia M. On the front velocity of gravity currents. J Fluid Mech 2007;586:1–39.
[9] Cortese T, Balachandar S. High performance spectral simulation of turbulent flows in massively parallel machines with distributed memory. Intl J Supercomput Appl 1995;9:187–204.
[10] Dade WB, Huppert HE. Predicting the geometry of channelized deep-sea turbidites. Geology 1994;22(7):645–8.

[11] Dade WB, Huppert HE. A box model for non-entraining, suspension-driven gravity surges on horizontal surfaces. Sedimentology 1995;42:453–71.
[12] Fannelop TK, Waldman GD. Dynamics of oil slicks. AIAA J 1972;10(4):506–10.
[13] Felix M, Peakall J. Transformation of debris flows into turbidity currents: mechanisms inferred from laboratory experiments. Sedimentology 2006;53(1):107–23.
[14] Fisher RV. Features of coarse-grained, high-concentration fluids and their deposits. J Sediment Res 1971;41(4).
[15] Härtel C, Fredrik C, Mattias T. Analysis and direct numerical simulation of the flow at a gravity-current head. Part 2. The lobe-and-cleft instability. J Fluid Mech 2000;418:213–29.
[16] Huppert HE, Simpson J. The slumping of gravity currents. J Fluid Mech 1980;99:785–99.
[17] Hoult DP. Oil spreading on the sea. Ann Rev Fluid Mech 1972;4:341–68.
[18] Kuenen PH. Experimental turbidite lamination in a circular flume. J Geol 1966;74:523–45.
[19] Lowe DR. Sediment gravity flows: their classification and some problems of application to natural flows and deposits. SEPM Spec Pub 1979;27:75–82.
[20] Maxworthy T. The dynamics of sedimenting surface gravity currents. J Fluid Mech 1999;392:27–44.
[21] Meiburg E, Kneller B. Turbidity currents and their deposits. Ann Rev Fluid Mech 2010;42:135–56.
[22] Middleton GV. Experiments on density and turbidity currents: I. Motion of the head. Canad J Earth Sci 1966;3(4):523–46.
[23] Necker F, Härtel C, Kleiser L, Meiburg E. Mixing and dissipation in particle–driven gravity currents. J Fluid Mech 2005;545:339–72.
[24] Parker G, Fukushima Y, Pantin HM. Self-accelerating turbidity currents. J Fluid Mech 1986;171:145–81.
[25] Ross AN, Linden PF, Dalziel SB. A study of three-dimensional gravity currents on a uniform slope. J Fluid Mech 2002;453:239–61.
[26] Rottman JW, Simpson JE. Gravity currents produced by instantaneous releases of a heavy fluid in a rectangular channel. J Fluid Mech 1983;135:95–110.
[27] Simpson JE. Effects of the lower boundary on the head of a gravity current. J Fluid Mech 1972;53:759–68.
[28] Ungarish M. An Introduction to Gravity Currents and Intrusions. CRC Press; 2009.
[29] Zgheib N, Bonometti T, Balachandar S. Dynamics of non-circular finite-release gravity currents. J Fluid Mech 2015;783:344–78.
[30] Zgheib N, Bonometti T, Balachandar S. Propagation and deposition of non-circular finite release particle-laden currents. Phys Fluids 2015;27(8):086604.
[31] Zgheib N, Ooi A, Balachandar S. Front dynamics and entrainment of finite circular gravity currents on an unbounded uniform slope. J Fluid Mech 2016;801:322–52.